Microtubule organization and cell geometry

Panayiotis Foteinopoulos and Bela M. Mulder*
Institute AMOLF, Science Park 104, 1098XG Amsterdam, the Netherlands

(Received 5 April 2022; accepted 11 October 2022; published 16 November 2022)

A characteristic feature of nondividing animal cells is the radial organization of microtubules (MTs), emanating from a single microtubule organizing center (MTOC). As generically these cells are not spherically symmetric, this raises the question of the influence of cell geometry on the orientational distribution of microtubules. We present a systematic study of this question in a simplified setting where MTs are nucleated from a single fixed MTOC in the center of an elliptical cell geometry. Within this context we introduce four models of increasing complexity, each one introducing additional mechanisms that govern the interaction of the MTs with the cell boundary. In order, we consider the cases: MTs that can bind to the boundary with a fixed mean residence time (M0), force-producing MTs that can slide on the boundary towards the cell poles (MS), MTs that interact with a generic polarity factor that is transported and deposited at the boundary, and which in turn stabilizes the MTs at the boundary (MP), and a final model in which both sliding and stabilization by polarity factors is taken into account (MSP). In the baseline model (M0), the exponential length distribution of MTs causes most of the interactions at the cell boundary to occur along the shorter transverse direction in the cell, leading to transverse biaxial order. MT sliding (MS) is able to reorient the main axis of this biaxial order along the longitudinal axis. The polarization mechanism introduced in MP and MSP overrules the geometric bias towards bipolar order observed in M0 and MS, and allows the establishment of unipolar order either along the short (MP) or the long cell axis (MSP). The behavior of the latter two models can be qualitatively reproduced by a very simple toy model with discrete MT orientations.

DOI: 10.1103/PhysRevE.106.054408

I. INTRODUCTION

In a typical animal cell, microtubules play a major role in the intracellular bidirectional trafficking of molecules from the vicinity of the cell nucleus to the cell periphery (for a recent review see [1]). In support of this function, the microtubule cytoskeleton generically displays a radial spatial organization governed by a single microtubule organizing center (MTOC) which localizes to the nuclear envelope. The MTOC is the locus of protein complexes, such as γ-tubulin ring complexes, which serve to nucleate new MTs (for a recent review see [2]). These MTs subsequently grow outward towards the cell periphery in roughly uniformly distributed directions. MTOCs, depending on cell type, can support up to hundreds of MTs [3].

The question what happens when the MTs still connected to the MTOC reach the cell boundary has to date mostly been considered in the context of three biologically relevant phenomena.

The first phenomenon is the role of these *bound* MTs play in the localization of the MTOC itself. In the seminal work by Tran *et al.* [4], it was shown that MTs, by virtue of the polymerization forces they exert when in contact with the cell membrane, are able to robustly center the nucleus in fission yeast to which they are connected the so called by spindle pole bodies on the nuclear envelope that act as multiple MTOCs in this case. Later work focused on the question of the positioning of *in vitro* reconstituted MT-asters, the star-like structure of MTs emerging from an MTOC, in lithographically produced microchambers [5,6], with a view of understanding spindle pole positioning in cells (see, e.g., [7,8]). An important insight gained from this work, is that in more spherical cells pushing forces do not provide a robust centering. Centering is only obtained if pulling forces, exerted by, e.g., cortical dynein motor proteins, are also at play. Related is the observation that in a nonspherical cell the polymerization force exerted by a growing MT at the membrane inevitably has a tangential component causing MTs to slide, and thus reshaping the MT distribution within the cell [9,10].

The second phenomenon is the role MTs play in the positioning and orientation of the mitotic spindle in metaphase prior to division (for a review see [11]). In this situation there are actually two MTOCs connected by a structure formed by the subset of so-called polar MTs. The remaining MTs, called astral, interact with the cell boundary in a process which again involves both pushing and pulling forces, and a mechanical redistribution of MTs over the surface.

The third phenomenon is the possible role of MTs in setting up and maintaining cell polarity (for a recent review see, e.g., [12]). The paradigmatic example of a system of this type was first discovered in fission yeast, in which the polarity marker Tea1p is transported by the motor protein Tea2p along longitudinally oriented MTs and subsequently delivered on the apical membrane aided by the MT-end binding protein Mal3p [13,14]. As Tea1p is an example of a so-called microtubule associated protein (MAP), a large class of proteins that bind to MTs and are, e.g., able to alter their dynamics, it has

*mulder@amolf.nl

been speculated that this could form the basis of a robust and self-sustaining polarization mechanism in which MTs serve to transport factors to the membrane, that subsequently stabilize them and hence provide a positive feedback-loop maintaining their localization [15,16].

The previous work described above strongly focused on specific questions and geometries, and it is fair to say that we do not yet have a comprehensive understanding of how cell geometry influences the global distribution of MTs given various types of potential interactions of the MTs with the cell boundary. Here we aim to fill this gap by analyzing a number of models in which we vary the cell geometry, both in absolute size and relative to the mean length of the MTs and implement four distinct scenarios of MT-boundary interactions of increasing complexity. While by design these models sacrifice some elements of biological realism, they allow a systematic comparative study of the interplay between MT dynamics, cell shape and boundary effects.

Specifically, we consider the following models for MT-boundary interactions: (M0) MTs that can bind to the boundary with a fixed mean residence time, (MS) force-producing MTs that can slide on the boundary towards the cell poles, (MP) MTs that interact with a generic polarity factor that is transported and deposited at the boundary, and which in turn stabilizes the MTs at the boundary, and (MSP) a final model in which both sliding and stabilization by polarity factors is taken into account. In all cases we study these models through stochastic simulations. However, for model M0 we also obtain a full analytical solution, while for the two models involving polarity (MP and MSP), we construct stylized toy models that allow us to rationalize the observed behavior. For the models involving force-induced MT sliding, we employ a recently developed force-production mechanism that explicitly accounts for the effect of force on the speed of growth and the residence time of MTs at the membrane [17]. The two main questions we focus on are (i) whether the MTs are predominantly organized along the longer longitudinal axis or the shorter transverse axis of the cell and (ii) whether the symmetries of the cell shape are imposed on the MT organization, or whether this symmetry can be broken, yielding a polarized state.

To render the analysis tractable, we make a number of simplifying assumptions. The first is to disregard the complexities of MTOC positioning as discussed above. We therefore consider only a single MTOC whose position is fixed to the geometrical center of the cellular geometry. This implies that we assume that an effective central positioning mechanism is already in place and is *not* perturbed by the additional mechanisms of MT-boundary interactions we implement. For the two models in which force production is important (MS and MSP), we can moreover show that given our model of MT dynamics there is a net centering force in the steady state. The main virtue of this assumption is that it allows us to more straightforwardly disentangle the differential effects on the global organization of the MTs due to differences in geometry and/or boundary conditions. Second, we disregard the possibility of MT buckling. Including this effect would require the implementation of a length-dependent buckling force and a challenging analysis of the postbuckling force orientations. For simplicity's sake we decided to forego this additional level of complexity. Finally, we restrict ourselves to a 2D elliptical cell geometry. The choice for an elliptical shape is one of convenience, both analytically and computationally. An ellipse shares the biaxial symmetry, generated by two orthogonal reflections, common to the shape of many elongated cells. It is therefore well suited to answer the symmetry-related questions we pose. The choice for 2D affords computational advantages that allow for a much more extensive range of conditions to be addressed through stochastic simulations than would be feasible in 3D. Moreover, our previous work [16] has explicitly shown that the effect of dimensionality on symmetry-breaking mechanisms involving polarity factors (relevant to models MP and MSP) is weak. In the Discussion we will revisit these assumptions.

The paper is organized as follows: in Sec. II we introduce our modeling framework, the cell geometry, the observables used (Sec. II A), and introduce the four models we consider (Sec. II B). In Sec. III we collect our results on the four models in order: M0 (III A), MS (III B), MP (III C), and MSP (III D). In Sec. III E we rationalize and compare the results on models MP and MSP with the aid of a simple toy model. We end with a discussion in Sec. IV. In three appendices we collect a number of technical details on the derivation of the MT dynamical equations underpinning model M0 (Appendix A), the implementation of the polarization mechanism in the presence of force production in model MSP (Appendix D), and an in-depth description of our toy model (Appendix E).

II. MODELING FRAMEWORK

A. Cell geometry and MT dynamics

We consider a pointlike idealized MTOC located at the center of an elliptical cell, with a major axis of half-length b, and minor axis of half-length $a < b$. Orientation of MTs in this geometry is specified by the azimuthal angle φ, defined with respect to the positive major half-axis. We will call the direction along the major axis *longitudinal* and the one along the minor axis *transverse*.

Each MT is nucleated by a nucleation complex located at the MTOC, and we fix the total number of these complexes, and hence the total number of MTs in the system, to be M. If a nucleation site is unoccupied it will nucleate a new growing MT with rate r_{n}. It is conceptually convenient to consider an unoccupied nucleation site as a *dormant* MT, waiting to be nucleated. We will consider two assumptions on the distribution of nucleation angles, both consistent with isotropicity of the overall nucleation pattern. The first, the *homogeneous* scenario, assumes each nucleation complex to fixedly point in a given direction, and that these directions have constant angular density m, and hence $M = 2\pi m$. The second, the *random* scenario, does not assume a fixed orientation for the nucleation complexes, but has them fire in a randomly selected direction.

Once a MT has been nucleated, it follows the standard MT dynamical instability model [18], with growth speed v_+, shrinking speed v_-, catastrophe rate r_+, and rescue rate r_-. When a MT hits the cell boundary it stalls, remaining there until it detaches by switching to the shrinking state with a rate r_{u}. The length of a MT when it hits the boundary in a given

direction is given by $l_b(\varphi)$, the latter function encoding all the relevant information about the shape of the cell. For the ellipse this length is given by

$$l_b(\varphi) = \frac{ab}{\sqrt{a^2\cos^2\varphi + b^2\sin^2\varphi}}. \quad (1)$$

We focus on the steady state of these systems, in which the orientational distribution of MTs can be described by the following quantities:

- $m_0(\varphi)$: The density (per angle) of *dormant* MTs pointing in the direction φ at time t in the homogeneous nucleation scenario.
- M_0: The number of dormant MTs in the random nucleation scenario.
- $m_+(l,\varphi)$: The density (per angle per unit length) of *growing* MTs of length l.
- $m_-(l,\varphi)$: The density (per angle per unit length) of *shrinking* MTs of length l.
- $m_a(l,\varphi) = m_+(l,\varphi) + m_-(l,\varphi)$: The density (per angle per unit length) of *active* MTs of length l
- $m_b(\varphi)$: The density (per angle) of MTs *bound* to the surface.

We also consider the associated length densities

$$L_a(\varphi) = \int_0^\infty dl\, l\, m_a(l,\varphi), \quad (2)$$

$$L_b(\varphi) = l_b(\varphi) m_b(\varphi), \quad (3)$$

$$L(\varphi) = L_a(\varphi) + L_b(\varphi). \quad (4)$$

To characterize the degree of orientational ordering of the MTs, we use two order parameters. The first measures the degree of *polar* ordering in the frame of the cell geometry. It is defined as

$$\mathbf{S}_1 = (\langle\cos\varphi\rangle, \langle\sin\varphi\rangle), \quad (5)$$

where throughout the equilibrium average is defined through

$$\langle f(\varphi)\rangle = \frac{\int_0^{2\pi} d\varphi\, f(\varphi)\, l(\varphi)}{\int_0^{2\pi} d\varphi\, l(\varphi)}, \quad (6)$$

i.e., we focus on the distribution of MT length, or equivalently tubulin mass. When convenient, the scalar order parameter $S_1 = |\mathbf{S}_1|$ can be used as a measure of the magnitude of polar ordering, irrespective of its orientation. The second-order parameter measures the degree of *bipolar* ordering and is defined as

$$\mathbf{S}_2 = \begin{pmatrix} \langle\cos 2\varphi\rangle & \langle\sin 2\varphi\rangle \\ \langle\sin 2\varphi\rangle & -\langle\cos 2\varphi\rangle \end{pmatrix}. \quad (7)$$

Here it is convenient to introduce the scalar order parameter $S_2 = (\mathbf{S}_2)_{xx} = \langle\cos 2\varphi\rangle$. When $S_2 > 0$ the ordering is predominantly along the major axis (*longitudinal*), while for $S_2 < 0$ the ordering is along the minor axis (*transverse*).

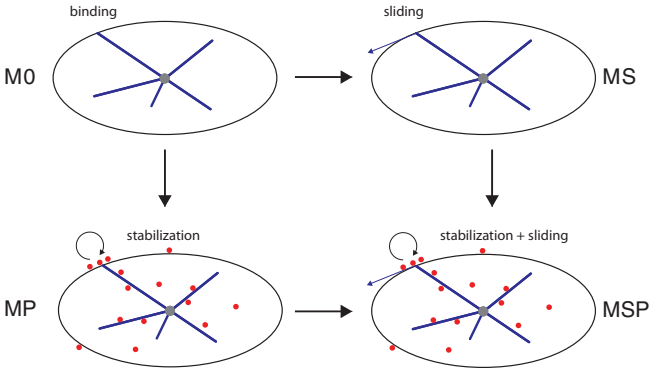

FIG. 1. Schematic of the four models considered. Microtubules (blue lines) are nucleated from a fixed MTOC (gray circle) at the center of the cell and extend towards the cell membrane (black ellipse). Polarity factors (red circles) when present, can either be free or bound to the microtubules and delivered to the membrane.

B. Models

We will consider four models of increasing complexity describing the interactions of the MTs with the boundary of our model cell. These models are schematically illustrated in Fig. 1.

Model M0: In this model, a growing MT that hits the boundary is stalled for a time set by an *unbinding rate*, after which it unbinds into the shrinking state.

Model MS: In this model, a growing MT that hits the boundary starts exerting a force. The tangential component of the polymerization force exerted by the MT on the boundary then causes the MT to *slide* towards the nearest cell pole, an effect counteracted by an (effective) friction force. At the same time, the rate at which the MT grows is slowed and its catastrophe rate is increased, both in a force-dependent manner.

Model MP: In this model we introduce a species of effector molecules we dub *polarity factors* (PFs). The PFs can bind to the MTs, which transport them towards the cell boundary. Once deposited there, they diffuse away and can reenter the cell interior at a given rate. The PFs in the boundary stabilize the bound MTs in a density-dependent manner, in this way creating a positive polarization-inducing feedback loop.

Model MSP: In this final model both the force-induced sliding mechanism, and the PF-induced polarization mechanism are active, yielding a model with maximal coupling to the cell boundary and its geometry.

III. MODELS AND RESULTS

A. Model M0: Fixed mean residence time at boundary

In this first model, which will serve as the default case to which the other models can be compared, the only effect on MTs reaching the cell boundary is that they enter a *bound* state, in which they are stalled. Release from this bound state occurs at a constant location-independent unbinding rate r_u. This mimics a generic nonspecific interaction between the MT tip and the membrane, which by varying the value of r_u ranges from repulsive ($r_u \gg 1$) to (hyper)stabilizing ($r_u \sim 0$). The model is schematically illustrated in Fig. 2.

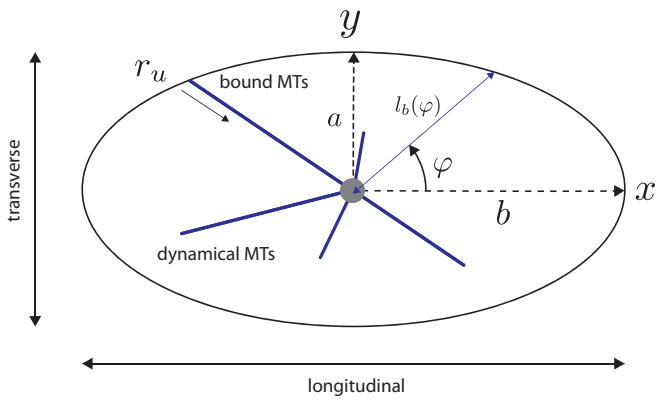

FIG. 2. Model M0: Dynamical MTs (blue lines) are isotropically nucleated from a fixed MTOC (gray circle) at the center of the cell. MTs remain bound to the membrane (black ellipse) with residence time set by the unbinding rate r_u. Also indicated are the coordinate frame employed throughout and the two named directions characterizing the cell geometry.

1. Analytical approach

We focus on the behavior of the relevant MT densities as introduced in Sec. II A in the steady state. The relevant equations follow from the time-dependent ones, which are presented in detail in Appendix A. For the growing, shrinking, and bound MTs, respectively, we have the balance equations

$$v_+\partial_l m_+(l,\varphi) = r_- m_-(l,\varphi) - r_+ m_+(l,\varphi), \tag{8}$$

$$-v_-\partial_l m_-(l,\varphi) = -r_- m_-(l,\varphi) + r_+ m_+(l,\varphi), \tag{9}$$

$$v_+ m_+(l_b(\varphi),\varphi) = r_u m_b(\varphi). \tag{10}$$

The behavior of the dormant MTs depends on the nucleation scenario, and we have

$$r_n m_0(\varphi) = v_- m_-(l=0,\varphi), \tag{11a}$$

$$r_n M_0 = \int_0^{2\pi} d\varphi\, v_- m_-(l=0,\varphi), \tag{11b}$$

where throughout the a-sublabeled equations will refer to the homogeneous nucleation case, and the b-sublabeled ones to the random nucleation case. These equations are supplemented by boundary conditions. At the cell boundary we must have

$$v_- m_-(l_b(\varphi)) = r_u m_b(\varphi), \tag{12}$$

while at $l = 0$ we have

$$v_+ m_+(l=0,\varphi) = r_n m_0(\varphi), \tag{13a}$$

$$v_+ m_+(l=0,\varphi) = r_n \frac{M_0}{2\pi}. \tag{13b}$$

Adding Eqs. (8) and (9) gives

$$\partial_l[v_+ m_+(l,\varphi) - v_- m_-(l,\varphi)] = 0. \tag{14}$$

Combining Eqs. (10) and (12), yields

$$v_+ m_+(l_b(\varphi),\varphi) = v_- m_-(l_b(\varphi),\varphi), \tag{15}$$

which shows that the constant of integration in Eq. (14) vanishes, and so we get

$$v_+ m_+(l,\varphi) = v_- m_-(l,\varphi). \tag{16}$$

This allows us to eliminate $m_-(l,\varphi)$ in Eq. (8) and solve it using either Eq. (13a) or (13b), yielding

$$m_+(l,\varphi) = \frac{r_n}{v_+} m_0(\varphi) e^{-l/\bar{l}}, \tag{17a}$$

$$m_+(l,\varphi) = \frac{r_n}{v_+}\frac{M_0}{2\pi} e^{-l/\bar{l}}, \tag{17b}$$

where

$$\bar{l} = \left(\frac{r_+}{v_+} - \frac{r_-}{v_-}\right)^{-1} \tag{18}$$

is the mean length of free MTs i.e., in the absence of boundaries [18]. From Eq. (10) we immediately get

$$m_b(\varphi) = \frac{v_+}{r_u} m_+(l_b(\varphi),\varphi). \tag{19}$$

The final unknowns, pertaining to the dormant MTs, can now be obtained from the appropriate conservation laws, which read

$$m = m_0(\varphi) + \int_0^{l_b(\varphi)} dl\,[m_+(l,\varphi) + m_-(l,\varphi)] + m_b(\varphi), \tag{20a}$$

$$M = 2\pi m = M_0 + M_a + M_b, \tag{20b}$$

where

$$M_a = \int_0^{2\pi} d\varphi \int_0^{L(\varphi)} dl\,[m_+(l,\varphi) + m_-(l,\varphi)], \tag{21}$$

$$M_b = \int_0^{2\pi} d\varphi\, m_b(\varphi) \tag{22}$$

are the total number of active and bound MTs in the system, respectively. Inserting the results for $m_+(l,\varphi)$, $m_-(l,\varphi)$ and $m_b(\varphi)$ in Eqs. (20a) and (20b) and introducing the convenient single MT "partition function"

$$Z(\varphi) = 1 + r_n\left(\frac{1}{v_+} + \frac{1}{v_-}\right)\bar{l}(1 - e^{-l_b(\varphi)/\bar{l}}) + \frac{r_n}{r_u} e^{-l_b(\varphi)/\bar{l}}, \tag{23}$$

we find

$$m = m_0(\varphi) Z(\varphi), \tag{24a}$$

$$M = M_0 \tilde{Z}, \tag{24b}$$

where throughout we use the tilde to denote the *unweighted* average over angles, i.e.,

$$\tilde{f} \equiv \frac{1}{2\pi}\int_0^{2\pi} d\varphi\, f(\varphi).$$

These results have a natural interpretation in terms of the following timescales: $t_0 = \frac{1}{r_n}$, the mean residence time in the dormant state, $\bar{t} = (\frac{1}{v_+} + \frac{1}{v_-})\bar{l}$, the mean lifetime of an unperturbed MT, $t_b = \frac{1}{r_u}$, the mean residence time at the cell boundary, and the quantity

$$F_b(\varphi) = e^{-l_b(\varphi)/\bar{l}}, \tag{25}$$

which can interpreted as the probability that a MT reaches the boundary in the direction φ. With these definitions we can write

$$Z(\varphi) = \frac{t_0 + [1 - F_\mathrm{b}(\varphi)]\bar{t} + F_\mathrm{b}(\varphi)t_\mathrm{b}}{t_0} \equiv \frac{t_\mathrm{tot}(\varphi)}{t_0}, \quad (26a)$$

$$\tilde{Z} \equiv \frac{\tilde{t}_\mathrm{tot}}{t_0}, \quad (26b)$$

where t_tot is interpreted as the total time spent in a single lifespan of a MT starting in the dormant state (t_0), spending a time t_b bound to the surface with probability F_b and behaving as an unperturbed MT with probability $1 - F_\mathrm{b}$. We now readily find the distribution of (i) the dormant MTs

$$m_0(\varphi) = m\frac{t_0}{t_\mathrm{tot}(\varphi)}, \quad (27a)$$

$$M_0 = M\frac{t_0}{\tilde{t}_\mathrm{tot}}, \quad (27b)$$

(ii) the active MTs

$$m_\mathrm{a}(l, \varphi) = m\frac{\bar{t}}{t_\mathrm{tot}(\varphi)}\frac{e^{-l/\bar{l}}}{\bar{l}}, \quad (28a)$$

$$m_\mathrm{a}(l, \varphi) = \frac{M}{2\pi}\frac{\bar{t}}{\tilde{t}_\mathrm{tot}}\frac{e^{-l/\bar{l}}}{\bar{l}}, \quad (28b)$$

and finally (iii) the bound MTs

$$m_\mathrm{b}(\varphi) = m\frac{t_\mathrm{b}}{t_\mathrm{tot}(\varphi)}F_\mathrm{b}(\varphi), \quad (29a)$$

$$m_\mathrm{b}(\varphi) = \frac{M}{2\pi}\frac{t_\mathrm{b}}{\tilde{t}_\mathrm{tot}}F_\mathrm{b}(\varphi). \quad (29b)$$

Intriguingly, when $\bar{t} = t_\mathrm{b}$, we have $t_\mathrm{tot}(\varphi) = \tilde{t}_\mathrm{tot} = t_0 + \bar{t}$. In this case the two nucleation scenarios lead to exactly the same results. Intuitively this can be understood as follows. Due to the fact that the MT dynamics is Markovian, the lifetime $\bar{t}$ is also equal to the *return time*, i.e., the time it takes on average for a growing MT to return to its initial length in the shrinking state. So, whether a MT is kept at the boundary in the stalled state for a time $\bar{t}$, or is free to propagate beyond the boundary and returning after a time $\bar{t}$, has no impact on the distribution within the boundary. From the perspective of the MTOC the dynamics of departing and returning MTs is as if they are launched into unbounded space in which no direction is favored, which removes the distinction between the two nucleation scenarios. The resulting interior MT distributions are simply those obtained by "cropping" the isotropic distribution to the region defined by the cell, while the distribution on the boundary is the radial projection of the distribution outside the cell onto the surface.

With the results on the MT number distributions, we are finally in a position to give the sought-after length distribution:

$$l(\varphi) = m\frac{\bar{t}\{\bar{l} - [\bar{l} + l_\mathrm{b}(\varphi)]F_\mathrm{b}(\varphi)\} + t_\mathrm{b}l_\mathrm{b}(\varphi)F_\mathrm{b}(\varphi)}{t_\mathrm{tot}(\varphi)}, \quad (30a)$$

$$l(\varphi) = \frac{M}{2\pi}\frac{\bar{t}\{\bar{l} - [\bar{l} + l_\mathrm{b}(\varphi)]F_\mathrm{b}(\varphi)\} + t_\mathrm{b}l_\mathrm{b}(\varphi)F_\mathrm{b}(\varphi)}{\tilde{t}_\mathrm{tot}}. \quad (30b)$$

TABLE I. Basic dynamical parameters of MTs used throughout.

Parameter	Symbol	Value	Reference
Growth speed	v_+	$0.018\,\mu\mathrm{ms}^{-1}$	[19]
Shrinkage speed	v_-	$0.040\,\mu\mathrm{ms}^{-1}$	[19]
Nucleation rate	r_n	$0.05\,\mathrm{s}^{-1}$	[20]
Catastrophe rate	r_+	$0.0078\,\mathrm{s}^{-1}$	[19]
Rescue rate	r_-	$0.0016\,\mathrm{s}^{-1}$	[19]

2. Predictions from the theory

We now use the theory derived above to map out the behavior of model M0. As our focus throughout is on the influence of the geometry and the boundary interactions, we a priori fix the relevant dynamical parameters of the MTs to a set of generic ones chosen on the basis of experimental data, and shown in Table I. First, and foremost, these parameters fix the mean length the MTs would have in the absence of any confining boundary given by Eq. (18) to $\bar{l} = 2.54\,\mu\mathrm{m}$.

The first question we address is the influence of the overall scale of the cell, as compared to $\bar{l}$, on the organization of the MTs. Since the interactions of the MTs with the boundary do not depend on the location on the boundary, we expect the MT distributions to follow the biaxial symmetry of the cell. We therefore compare the value of the bipolar order parameter S_2 for different values of the boundary residence time t_b at a fixed aspect ratio $b/a = 4$ for different absolute sizes of the cell, chosen such that three distinct relevant cases are covered: $a < b < \bar{l}$, $a < \bar{l} < b$, and $\bar{l} < a < b$.

The main takeaway of the results shown in Fig. 3(a) is that in the random nucleation scenario the order parameter S_2 varies more strongly as a function of the residence time than in the homogeneous nucleation scenario. This is readily understood as in the random scenario the MTs can be effectively redistributed over the possible orientations if they are "sequestered" at the boundary, whereas in the homogeneous scenario fixed numbers of MTs are apportioned to each interval of angles. Another striking result is that in the largest cells, where MTs will hardly ever reach the longitudinal poles, S_2 will become negative in both scenarios as the distribution is dominated by MTs captured at the boundary on the transverse short axis. We thus have an ordered state for which $\mathbf{S}_1 = 0$ and $S_2 < 0$. We denote the symmetry of this state $D_2^\perp$, where D_2 is the standard Schönfliess nomenclature for the symmetry of a 2D rectangular shape, and the superscript $\perp$ indicates that the major axis of ordering is the transverse one. This state is illustrated in the upper left panel of Fig. 11.

Since we are explicitly interested in the competition between the short and the long axis of the cell, we now choose to fix the short semiaxis to $a = 1\,\mu\mathrm{m}$, and consider three cases in which the probability of MTs reaching the pole in the longitudinal direction is high ($b < \bar{l}$), average ($b = \bar{l}$), and low ($b > \bar{l}$), respectively. The results are given in Fig. 3(b) showing once again that the random nucleation scenario displays the largest sensitivity to the residence time at the boundary.

On the basis of these results and the pragmatic need to reduce the parameter space addressed by our study, we now make the following choices which we will apply throughout

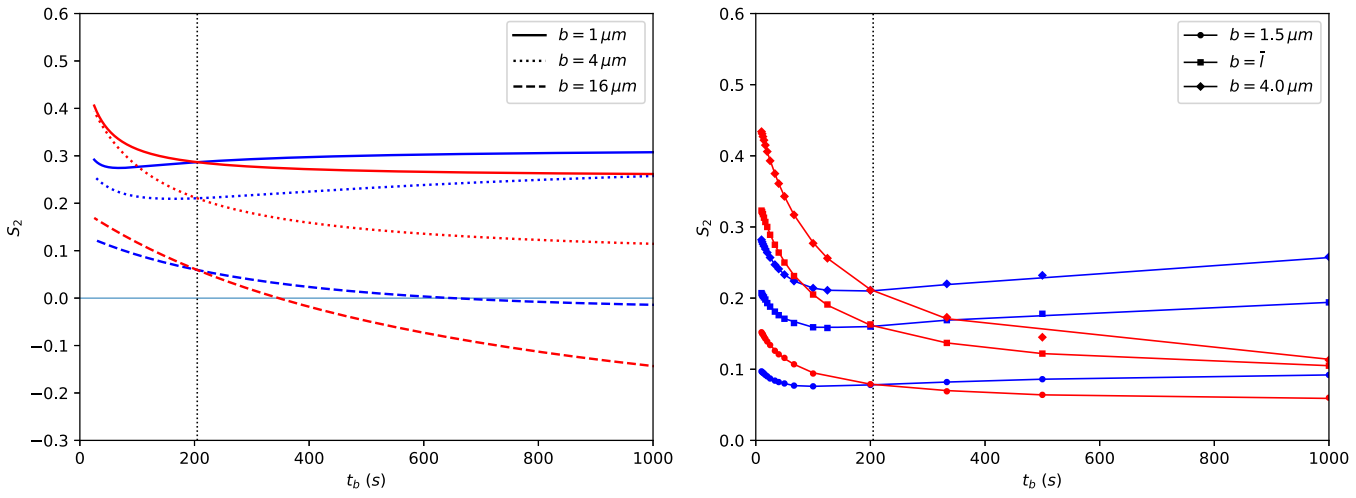

FIG. 3. Model M0: Order parameter S_2 as a function of the mean residence time at the cell boundary t_b, in both nucleation scenarios: homogeneous (blue) and random (red). The vertical line at $t_b = 204.8$ s indicates the special value of the boundary residence time at which the difference between the nucleation scenarios vanishes. (a) For a fixed aspect ratio $b/a = 4$. Cases: (i) $a = 0.25\,\mu$m, $b = 1\,\mu$m (solid), (ii) $a = 1\,\mu$m, $b = 4\,\mu$m (dotted), (iii) $a = 4\,\mu$m, $b = 16\,\mu$m (dashed). (b) For different aspect ratios b/a setting $a = 1\,\mu$m and cases (i) $b = 1.5\,\mu$m, (ii) $b = \bar{l} = 2.54\,\mu$m and (iii) $b = 4\,\mu$m. The symbols indicate the values obtained by simulations. Error bars in the simulations are smaller than the symbols.

the rest of the study: (i) as it appears most sensitive probe of changes in the MT organization due to changes in the geometry and/or the boundary residence time, we adopt the random nucleation scenario, (ii) to explicitly address the competition between the two axes of the cell, we adopt $a = 1\,\mu$m ensuring that the cell boundary in the transverse direction is readily accessible to MTs, and (iii) as $t_b = 100$ s lies in the middle of the regime of largest sensitivity, we choose this value of the boundary residence time to be our baseline, close to the experimentally reported value of $\approx$90 s in fission yeast [4].

3. Comparison with simulations

In order to set up the core algorithm which will be used to simulate the MT dynamics in the rest of the study, we perform standard fixed time step stochastic simulations of model M0. These simulations are then validated against the analytical predictions of the previous section.

In the simulations, individual MTs are modeled as objects in one of the possible states DORMANT, GROWING, SHRINKING, and BOUND. At each time step the probability of transitioning to another state is calculated and sampled. If the MT remains in its state its length is updated as appropriate. The possible transitions are DORMANT $\rightarrow$ GROWING, with rate r_n, GROWING $\rightarrow$ BOUND, which occurs whenever the length of the MT is equal to the distance between MTOC and cell boundary in the direction in which it is growing, and BOUND $\rightarrow$ SHRINKING, with rate r_u, GROWING $\rightarrow$ SHRINKING (catastrophes), with rate r_+, SHRINKING $\rightarrow$ GROWING (rescues), with rate r_-, and finally, SHRINKING $\rightarrow$DORMANT, which occurs whenever a shrinking MT hits zero length. In the homogeneous nucleation scenario, each MT is assigned a fixed angle $\varphi_m = m\,2\pi/M$, $m = 0, 1, \ldots, M-1$. In the random scenario, a random angle is chosen upon a nucleation event. Here we chose to simulate $M = 1000$ MTs and use a time step of $\Delta t = 0.5$ s. The dynamical parameters of the MTs are the ones given in Table I. Here, as in the rest of the study, we use the order parameters defined in Sec. II A as reporters on the global organization of the MTs. In Appendix B we show a single representative comparison between the distribution function $l(\varphi)$ obtained by solving Eq. (30) and the distribution measured in simulations, from which the order parameters are then derived.

B. Model MS: Force generation and boundary sliding

In this second model we take into account that, due to continued polymerization, a MT stalled at the cell boundary exerts a force in the direction in which it is oriented [21]. This force is counterbalanced by a normal force exerted by the cell surface. The latter force has a component orthogonal to the MT, causing it to slide along the surface [10]. At the same time, one expects that the growth speed as well as the catastrophe rate of bound MT are influenced by the loading force [22]. Here we will take both these effects into account using a recently developed model of dynamic force generation, which is parametrized using data on yeast cells [17]. A generic friction parameter then controls the degree to which sliding contributes to the overall MT organization. This model is illustrated in Fig. 4.

1. Dynamic force generation mechanism

We adopt the force generation model described in [17]. This model is based on the phenomenological notion of "stored length," which is built up when the MT continues to grow after coming into contact with the boundary. That MTs are able to grow due to thermal fluctuations, in spite of the fact that they are in contact with a boundary, is a key ingredient of the standard Brownian ratchet model of polymerization forces [23]. The stored length, defined as the difference between the

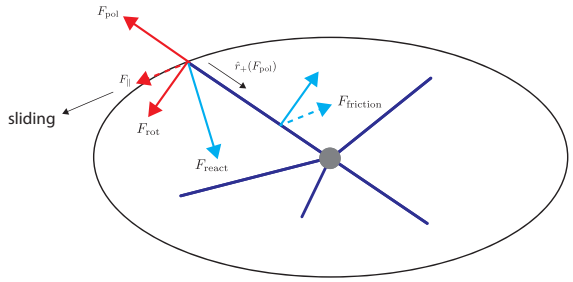

FIG. 4. Model MS: The polymerization force $F_{\rm pol}$ due to growth of the MT is counteracted by the normal force $F_{\rm react}$. This force has a component $F_{\rm rot}$ which acts to rotate the filament, but is in turn balanced by friction with the intracellular medium. This results in a sliding motion along the cell boundary, driven by the tangential force $F_{\parallel}$ and counteracted by the effective friction force $F_{\rm friction}$. The residence time of the MT at the boundary is influenced by their degree of force loading, through a force-dependent catastrophe rate $\hat{r}_+(F_{\rm pol})$.

length of MT and the distance between the nucleation point and the point of contact with the boundary, is interpreted as the source of a linear "expansion" force countering the compression at the boundary given by

$$F_{\rm pol}(l, L) = k(l - L), \tag{31}$$

where l is the length of the MT, L the distance between MTOC and the cell boundary and k an effective compression modulus which governs the magnitude of the generated force. We next assume that the microscopic dynamics of the MT, involving the addition and removal of individual tubulin subunits, is fast compared to the growth process, and that the off-rate by which tubulin subunits detach from the MTs is small with respect to the on-rate by which subunits attach to the MT. Under these assumptions, the growth speed quasistatically decreases as [24]

$$\hat{v}_+(F_{\rm pol}) = v_+ e^{-\beta d F_{\rm pol}}, \tag{32}$$

where $\beta = (k_B T)^{-1}$ is the inverse temperature in units of the Boltzmann constant and d is the microscopic step size of the growth process. This parameter can be determined phenomenologically on the basis of measured force-velocity relations. The value suggested by Foethke *et al.* [25], in the context of a similar model, is presented as $\beta d = 1/f_{\rm s}$ with the characteristic force $f_{\rm s} = 1.67\,{\rm pN}$ determining the sensitivity of the MT growth to the opposing force. Throughout we will denote quantities in the force-loaded state by a hat ($\hat{\cdot}$).

To model the effect that the catastrophe rate should increase when in contact with the boundary, the assumption is made that the linear relation observed between growth speed and mean time to catastrophe for freely growing MTs [22] also holds instantaneously for loaded MTs. This implies that

$$\hat{t}_+(F_{\rm pol}) = \frac{1}{\hat{r}_+(F_{\rm pol})} \propto \hat{v}_+(F_{\rm pol}), \tag{33}$$

which yields

$$\hat{r}_+(F_{\rm pol}) = r_+ e^{F_{\rm pol}/f_{\rm s}}. \tag{34}$$

Moreover, we assume that in the loaded state, $l > L$, no rescues are possible, so that once a catastrophe occurs in this regime the MT will shrink to the unloaded state $l \leqslant L$ and that the shrinkage speed is unaffected by the loading.

For nonspherical cells, the growth-driven polymerization force $F_{\rm pol}$ is generically not perpendicular to the boundary (please refer to Fig. 4 for geometry of the forces involved). In case there is no direct friction with the cell membrane, this force is counteracted by a normal force $F_{\rm react}$, which has a component $F_{\rm rot}$ perpendicular to the MT, causing it to rotate. This latter force in turn is counteracted by the friction of the motion of the MT through the intracellular medium. In principle this friction force $F_{\rm friction}$ is weakly length-dependent, which we ignore here. As the MT rotates, it also expands releasing the stored length, causing it to slide along the surface. This motion appears to be driven by the tangential component $F_{\parallel}$ of the rotatory force, which by elementary geometry is equal to the tangential component of the polymerization force. Velocity and force of this sliding motion are then connected by the viscous equation of motion

$$F_{\parallel} = -\xi v_{\parallel}, \tag{35}$$

where ξ is an effective drag coefficient.

2. Implementation

In order to implement force production and sliding into our stochastic simulations, we replace the BOUND state of model M0, by the state PUSHING. In the latter state the MT grows with speed $\hat{v}_+(F_{\rm pol})$ given by Eq. (32) and experiences a catastrophe rate given by $\hat{r}_+(F_{\rm pol})$ given by Eq. (34), where the polymerization force is found from the current length and orientation through Eq. (31). If at the end of a time step the MT remains in the PUSHING state, the tangential force $F_{\parallel}$ it experiences is calculated using Eq. (31) by projecting onto the tangent line to the elliptical boundary at the point of contact determined by its current orientation φ. The MT is then rigidly rotated over an angle $\Delta\varphi = F_{\parallel}/[\xi L(\varphi)]\Delta t$. Ignoring catastrophes, the stable points of this rotation are the poles of the ellipse on the long axis, where the tangential component of the forces disappears. By the same token, generically $L(\varphi + \Delta\varphi) > L(\varphi)$ so that this motion also relaxes the magnitude of the driving force.

In order to facilitate comparison between the models MS and M0, we must choose a suitable value for the effective modulus k. We do this by requiring that in the absence of sliding, the mean time until catastrophe of a pushing MT equals the mean residence time set by the reference unbinding rate $r_{\rm u}$ discussed in Sec. III A 2. To be fully precise, the residence time should also include the time it takes a loaded MT to shrink to the unloaded state, but given that the shrinking speed is significantly larger than the growing speed, this would only amount to a small correction. The mean time to catastrophe in the force production model works out as [17]

$$\langle \tau_{\rm c} \rangle = \frac{1}{r_+}\sqrt{\pi}\sqrt{r_+\Phi}e^{r_+\Phi}{\rm erfc}(\sqrt{r_+\Phi}), \tag{36}$$

where

$$\Phi = \frac{f_{\rm s}}{2kv_+}, \tag{37}$$

and erfc is the complementary error function (see Ref. [26], table entry 8.250.4), and r_+ and v_+ are the force-free values

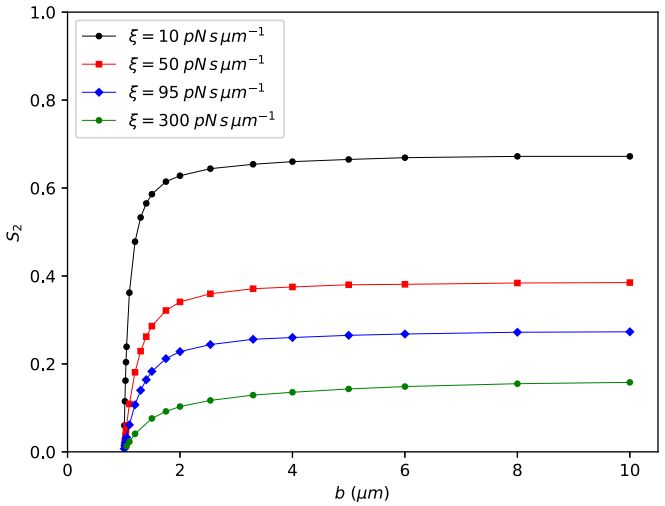

FIG. 5. Model MS: Order parameter S_2 for different aspect ratios by changing the long semiaxis b and for different values of the sliding drag coefficient ξ. Lines through the data points are guides to the eye.

of the catastrophe rate and the growth speed respectively. We now adjust k to achieve $\langle \tau_c \rangle = 1/r_u$ for the reference case $r_u = 0.01\,s^{-1}$, which yields $k = 0.3\,pN\mu m^{-1}$.

3. Simulation results

We apply our algorithm to different aspect ratios b/a of the cell and to different values of the sliding drag coefficients ξ. The simulation results for the order parameter S_2 are shown in Fig. 5. In all cases, we see that the sliding mechanism leads to robust biaxial order dominant along the longitudinal axis ($S_2 > 0$), with the degree of ordering increasing with decreasing friction, and reaching values significantly above those achieved in the reference Model M0 [cf. Fig. 3(b)]. We denote the symmetry of this type of ordered state by $D_2^{\parallel}$, and illustrate it in the upper right panel of Fig. 11.

While we have assumed at the outset that our MTOC is fixed in the geometrical center of the cell, it is of course a legitimate question to ask whether this central positioning is actually stable given that forces are at play that could potentially displace the MTOC. We therefore performed simulations in which the MTOC is displaced from the center and measured the resulting net force, showing that in our elongated geometry this force is centering and increases with increasing displacement from the center. We present these results in Appendix C.

C. Model MP: Molecular polarization mechanism

In this third model we add a MT-configuration dependent polarization mechanism to the basic model M0. The main additional ingredient of this model is the presence of a pool of effector proteins, which we dub polarity factors (henceforth PFs). These PFs start out cytosolic, i.e., in the cell interior, where they diffuse and bind to MTs. Bound PFs are transported in the plus-end direction along their host MTs towards the cell periphery. If their host MT is at the cell boundary, they can be delivered into the membrane, in which they diffuse until they unbind and recycle into the cell interior. The key

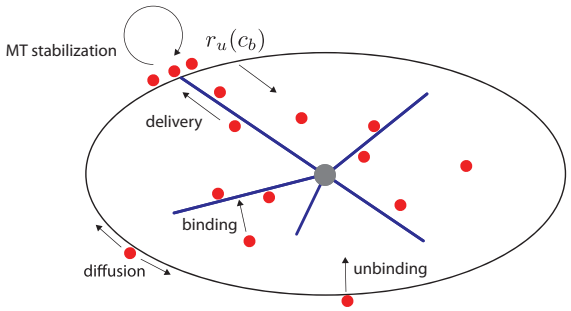

FIG. 6. Model MP: The effector species PF (red disks) binds to MTs over which they are transported. Bound MTs deliver PFs to the membrane, where they diffuse until they unbind to return to the cell interior. The residence time of bound MTs depends on the local density of PFs c_b in the membrane through the unbinding rate $r_u(c_b)$.

assumption of our polarization mechanism is that the residence time of the bound MTs depends on the local density of membrane-bound PFs setting up a positive feedback loop: the higher the local PF density, the longer a MT remains bound, the more PFs it delivers. As the total pool of PFs is finite, this also causes a global depletion effect, which represses the polarizing propensity of MTs in other parts of the cell. Conceptually this model thus belongs to the generic class of activator-depletion models (see [27] for a general overview), but distinguishes itself by employing the nondiffusible MTs as a mediator species. The model is schematically illustrated in Fig. 6.

1. Formalism and implementation

The model adopts the formalism developed in [16], where it was applied in a spherical cell geometry. Conservation of PFs implies that at any time

$$C = C_f(t) + C_m(t) + C_b(t), \tag{38}$$

where C is the total number of PFs, $C_f(t)$ the number of free PFs in the interior, $C_m(t)$ the number of PFs bound to MTs and $C_b(t)$ the number of PFs bound to the membrane. We assume the diffusion of the PFs in the cell interior to be very fast, so that their instantaneous distribution is spatially homogeneous, and that the kinetics of binding and unbinding to the MTs is so fast that an instantaneous binding equilibrium is established, allowing the linear density of PFs bound to MTs to be given by

$$c_m(t) = \frac{C_m(t)}{L(t)} = \frac{1}{L(t) + L_{\frac{1}{2}}}[C - C_b(t)], \tag{39}$$

where $L(t)$ is the total length of all MTs in the system, and $L_{\frac{1}{2}}$ a parameter that sets the affinity of the PFs for binding to the MTs. Calling the constant transport speed of PFs bound to MTs v_m, each membrane-bound MT delivers $v_m c_m(t)\Delta t$ PFs to the membrane per time step. Once in the membrane the PFs perform a standard diffusion and can unbind at a rate k_u, in which case they return to the interior pool. The coupling between membrane-bound PFs and membrane-bound MTs is implemented by the nonlinear dose-response function, which governs the MT unbinding rate as a function of the local PFs

TABLE II. Parameters used in the implementation of the polarization mechanism.

Parameter	Symbol	Value
Binding affinity PFs to MTs	$L_{\frac{1}{2}}$	150 μm
Transport speed PFs along MTs	v_m	0.81 μms^{-1}
Base MT unbinding rate	$r_u(0)$	0.01 s^{-1}
MT unbinding rate at PF saturation	$r_u(\infty)$	0.001 s^{-1}
Hill coefficient dose-response curve	p	5
Cross-over density dose-response curve	c_*	20bin^{-1}
Diffusion coefficient PFs	D	0.035 μm^2 s^{-1}
PF unbinding rate	k_u	0.07 s^{-1}

density c_b,

$$r_u(c_b) = [r_u(0) - r_u(\infty)]\frac{1}{1+\left(\frac{c_b}{c_*}\right)^p} + r_u(\infty), \tag{40}$$

where $r_u(0)$ is the MT-unbinding rate in the absence of PFs, $r_u(\infty)$ the MT-unbinding rate at PF oversaturation, c_* a cross-over density and p a Hill coefficient, which governs the steepness of the cross-over between the low- and high-density regimes.

In the simulations, the diffusion of the PFs in the membrane is implemented as a fixed time step continuous space Brownian motion obtained by sampling from the appropriate Gaussian propagator. The local density is evaluated by binning the PFs in the boundary, with an additional discrete noise suppressing averaging over a local neighborhood. For further details the reader is referred to [16]. The values of the additional parameters used are shown in Table II.

2. Simulation results

We simulated model MP for cellular geometries with two different aspect ratios: a less elongated, and hence more nearly circular, case with $b/a = 1.5$ and a more elongated case $b/a = 4$. The results are shown in Figs. 7(a) and 7(b), respectively. We see that in both cases there is a range of values for C, the total number of PFs in the system, for which polarization is observed. Since the number of MTs in contact with the boundary is largest along the short, transverse axis of the cell the polarization occurs along this axis. We therefore only plotted the component $|\mathbf{S}_{1,y}|$ of the vectorial order parameter $\mathbf{S}_1$. The absolute value is taken for convenience, as by reflection symmetry in the x axis, the polarization in the $-y$ direction is as likely as in the $+y$ direction. We denote the symmetry of this type of ordered state by $D_1^{\perp}$, where D_1 is the Schönfliess notation for the symmetry of a 2D figure with a single axis of reflection. The state is illustrated in the lower left panel of Fig. 11.

The most striking result is observed for the nonpolarized states in the more elongated cell [Fig. 7(b)]. For low values of C, where the polarization mechanism has not yet kicked in, the system responds to the geometry similarly to the reference Model M0 [cf. Fig. 3(b)], i.e., with a slight preference for longitudinal biaxial order ($S_2 > 0$). However, at high values of C when the polarization mechanism is no longer effective due to oversaturation, the system actually retains an "imprint" of the transverse polarization at intermediate values of C, by now settling on a transverse biaxial ordered state ($S_2 < 0$), with the major mass of the MT-length distribution oriented along the y axis.

D. Model MSP: Polarization mechanism and sliding

In this final model we combine the sliding mechanism of Model MS with the polarization mechanism of Model MP. We focus on the interplay between the tendency of sliding to create a bipolar MT organization along the long axis of the cell, and the tendency of the polarization mechanism to establish unipolar order. The model is schematically illustrated in Fig. 8.

1. Combining force production with the polarization mechanism

In order to connect the force-production mechanism of Model MS to the polarity-generation mechanism of Model

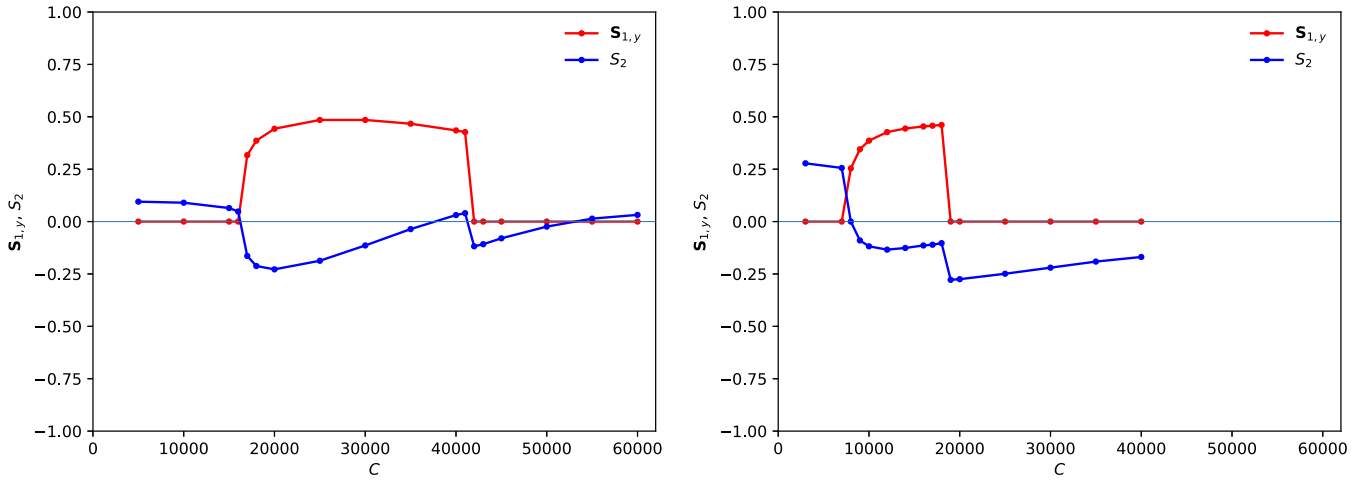

(a) (b)

FIG. 7. Model MP: Order parameters $|\mathbf{S}_{1,y}|$ and S_2 as functions of the total number C of polarity factors in the system for (a) $b = 1.5$ μm and (b) $b = 4$ μm.

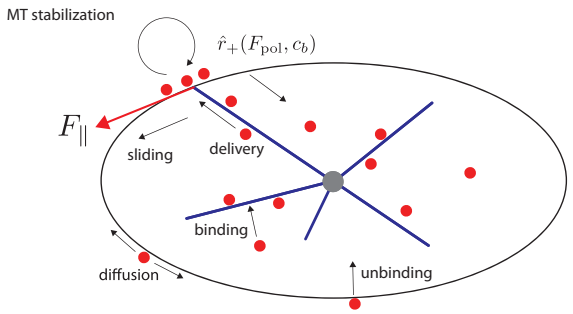

FIG. 8. Model MSP: Model that combines the polarization mechanism based on effector species PF (red circles) with polymerization-force induced sliding. The residence time of bound MTs depends on both the polymerization force and the local PF density through the catastrophe rate $\hat{r}_+(F_{\rm pol}, c_{\rm b})$.

MP, we chose to generalize the procedure adopted in Sec. III B 2 to link model MS to M0 through the mean-residence time. In this case we require that the mean time to catastrophe due to the force production mechanism $\langle\tau_{\rm c}\rangle$ tracks the nonlinear dependence of the unbinding rate on the PF density, i.e.,

$$\langle\tau_{\rm c}\rangle(c_{\rm b}) = \frac{1}{r_{\rm u}(c_{\rm b})}, \tag{41}$$

where $r_{\rm u}(c_{\rm b})$ is given by Eq. (40). Recalling Eqs. (36) and (37), we in principle have some freedom in which parameter to use to enforce this identity. We argue, however, that the most natural one is the unloaded catastrophe rate r_+, which most directly represents the intrinsic stability of the MT that is modulated by the presence of the PFs. In practice, we therefore solved [cf. Eq. (36)]

$$\frac{1}{r_{\rm u}(c_{\rm b})} = \frac{1}{r_+(c_{\rm b})}\sqrt{\pi}\sqrt{r_+(c_{\rm b})\Phi}e^{r_+(c_{\rm b})\Phi}\mathrm{erfc}[\sqrt{r_+(c_{\rm b})\Phi}] \tag{42}$$

for $r_+(c_{\rm b})$ over a range of $c_{\rm b}$ values, constructing a look-up table from which the appropriate value can be retrieved by interpolation when needed in the simulations. The details of this procedure are given in Appendix D.

2. *Simulation results*

In Fig. 9 we show the results of the simulations for two values of the aspect ratio of the cell plotting order parameters as functions of C, the total number C of PFs in the cell, for $\xi = 30\,\mathrm{pNs\mu m^{-1}}$. Since in this case, due to the efficacy of the sliding mechanism, the number of MTs in contact with the boundary is largest along the longitudinal axis of the cell, polarization, when it occurs, is along this axis. Here we therefore plotted only the component $|\mathbf{S}_{1,x}|$ of the vectorial order parameter $\mathbf{S}_1$, where, again for symmetry reasons, the absolute value is shown. We denote the symmetry of this polarized ordered state as $D_1^{\parallel}$. It is illustrated in the lower right panel of Fig. 11. In comparison with Model MP, the degree of polarization, which now piggybacks the intrinsic preference for longitudinal order already displayed in Model MS, is much more pronounced. At the same time, the impact of the polarization mechanism in the postpolarization high-C regime on the degree of biaxial order is significantly higher than that achievable by geometry [cf. Fig. 3(b)] or sliding (cf. Fig. 5) alone.

E. Toy models

Considering the observed behavior of the models MP and MSP, we can readily discern the critical factor that distinguishes the two cases: whether or not the interaction of MTs with the boundary is dominated, by virtue of the innate exponential length distribution of the MTs, by the most accessible shortest distance in the geometry, i.e., the transverse one in the elliptical geometry. This suggests that the observed behavior can be recapitulated in the setting of a highly simplified toy model that captures the essential ingredients at play. This model dispenses with the complexity due to to the continuous distribution of MT angles, and considers only a discrete number of directions. In the most generic case mimicking the

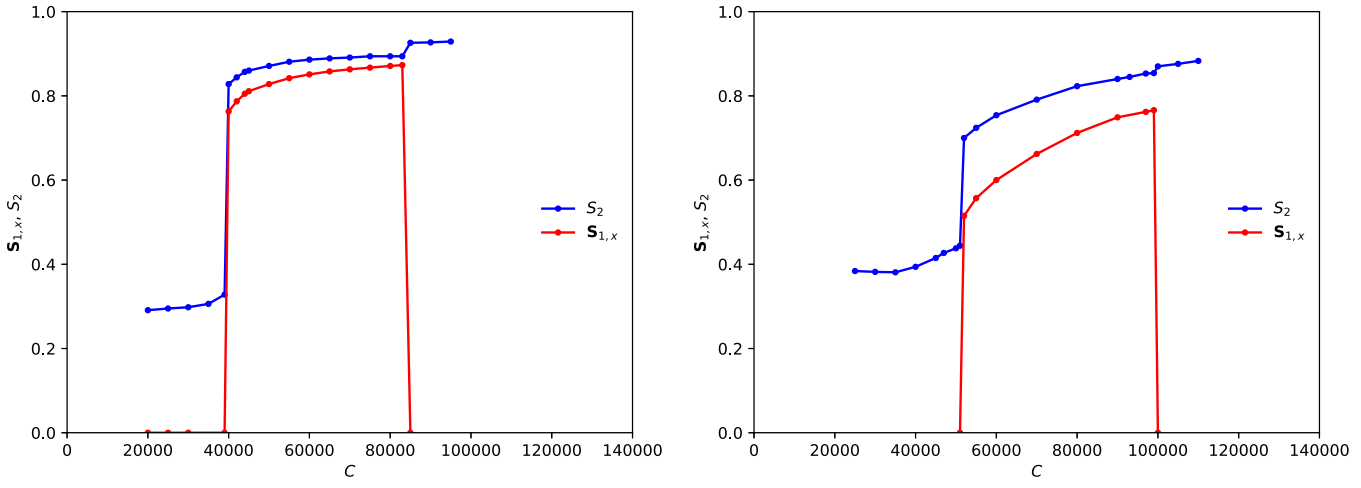

(a) (b)

FIG. 9. Model MSP: Order parameters $|\mathbf{S}_{1,x}|$ and S_2 as functions of the total number C of polarity factors in the system for (a) $b = 1.5\,\mu$m and (b) $b = 4\,\mu$m.

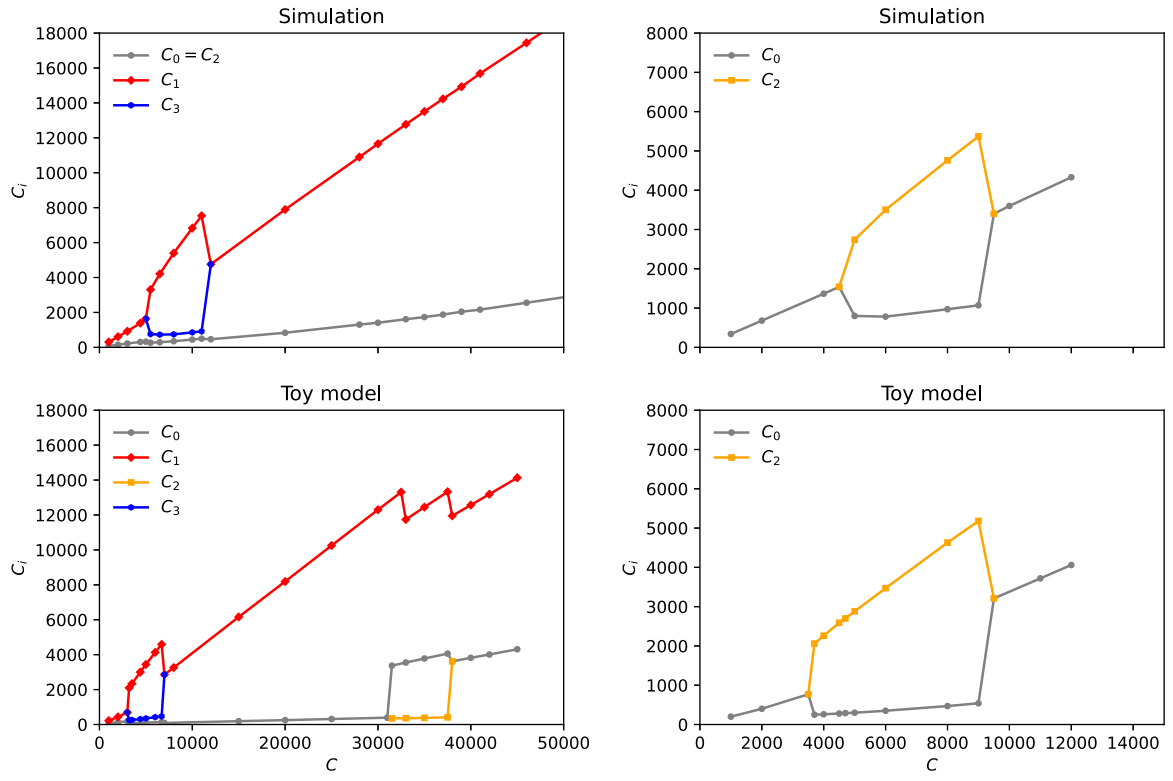

FIG. 10. (a) Model TOY-MP: Predictions for the (local) number of PFs C_i in each of the four membrane sectors in each as a function of the total number of PFs C of the toy model (below) compared to the full simulations (above). Here $C_* = 1000$. (b) Model TOY-MSP: Predictions for the (local) numbers of PFs C_i in the two halves of the membrane as a function of the total number of PFs C of the toy model (below) compared to the full simulations with drag coefficient $\xi = 1\,\mathrm{pNs\mu m^{-1}}$ (above).

behavior of model MP, we consider two opposing transverse orientations with a membrane at a distance a, and two opposing longitudinal orientations with the membrane at a distance b. Moreover, we remove any cross-talk due to PFs diffusing from one delivery point to another, effectively cutting the elliptical membrane into four disconnected sectors (see Fig. 15). The latter approximation is reasonable whenever the mean free diffusion length of PFs in the membrane is smaller than the distance between two delivery points, i.e., at a quarter of the cell circumference. We will call this model TOY-MP. In case we are mimicking the behavior of model MSP, where, specifically when the friction coefficient is not too high, we know that sliding will focus the majority of MTs along the longitudinal axis of the cell, a toy model with just two orientations opposing longitudinal directions can be expected to be a fair approximation, which we dub TOY-MSP. The details of the construction of these two toy models and our approach to numerically solve them are given in Appendix E.

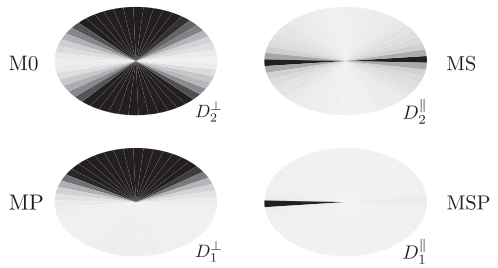

FIG. 11. Radial density plots of the density of bound microtubules $m_b(\phi)$ in the four models we considered, showing the distinct possible symmetries achievable. The average number of bound MTs were binned in 50 angular bins and mapped to a grayscale with black assigned to the maximum value. The geometry was $a = 1\,\mu\mathrm{m}$ and $b = 1.5\,\mu\mathrm{m}$. Details: Model M0: Unbinding rate $r_u = 0.01\,\mathrm{s}^{-1}$, Model MS: Drag coefficient $\xi = 50\,\mathrm{pNs\mu m^{-1}}$, Model MP: number of PFs $C = 30\,000$, Model MSP: number of PFs $C = 60\,000$. All other parameters as described in the main text.

We can directly compare the results of the toy models to the full simulation, if we ensure that the fixed nucleation rate in the toy models is adjusted to the observed steady-state overall nucleation rate in the simulations. As observables, we take the total number of PFs in each membrane sector. The results for model TOY-MP are presented in Fig. 10(a) and show that the toy model indeed reproduces the transverse polarization transition, albeit at a significantly lower number of total PFs. This stands to reason, as the PFs in the full model are far more dispersed over the membrane, in contrast to the toy models where they are highly focused, and hence act more strongly to stabilize the bound MTs. Strikingly, the toy model also predicts a possible longitudinal polarization transition, which occurs far beyond the point where the transverse polarization has already disappeared due to local saturation of the polarization mechanism. We did not observe such a transition in

the full simulations, possibly because it occurs for a much higher number of PFs than we choose to simulate here. Model TOY-MSP, with just two directions, appears even to semiquantitatively reproduce the full simulation data, as shown in Fig. 10(b).

IV. DISCUSSION

We have presented an exploration of the effects of nonspherical cell shape on the global distribution of MTs isotropically nucleated from a centrally located MTOC, a geometry that is a stylized version of the situation that pertains to a generic interphase eukaryotic cell, using four different models of increasing complexity. The main effect is revealed in the simplest model M0 in which the MTs have a generic interaction with the cell boundary that causes them to stall for a variable amount of time. As in steady-state MTs have an exponential length distribution, they are much more likely to interact with the cell boundary in the transverse equatorial direction, leading to a $D_2^{\perp}$ symmetry. This intrinsic orientational selection mechanism can be overruled if we allow MTs to slide driven by their intrinsic force-generating mechanism (Model MS), in which case the distribution can be reoriented towards the longitudinal direction, yielding a $D_2^{\parallel}$ symmetry. In both cases, the resulting distribution is bipolar with biaxial symmetry and conforms to the inversion symmetry of the cell shape. This strong coupling between the cell shape and MT distribution can itself be overridden by introducing an explicit polarization mechanism. This mechanism is mediated by polarity factors that depend on MTs for their delivery to the cell membrane and in turn stabilize the bound MTs increasing their residence time at the boundary, hence setting up a positive feedback loop. This breaks the inversion symmetry and creates either a polarized distribution in the transverse direction (Model MP) with symmetry $D_1^{\perp}$ or longitudinal direction (Model MSP) with symmetry $D_1^{\parallel}$. The various trade-offs involved are captured qualitatively, and in some cases even semiquantitatively, by a very simple, and potentially extendable, toy model that discretizes the orientations. In Fig. 11 we present a graphical summary of the four distinct MT organizations we have found. These are obtained by visualizing the steady-state density of surface-bound MTs as measured in simulations of the four models.

Obviously, the models presented here involve a number of clear (over)simplifications. The first one concerns the nature of the localization of the centrosome. In reality this structure is (i) eccentrically connected to the nuclear envelope, so that the nucleus will occlude a significant fraction of potential orientations for MTs, and (ii) not at a preordained location, but rather dynamically positioned. The latter effect has been studied extensively [5,6,9,10] and likely involves the interplay between pushing forces (generated by the MTs themselves) and pulling forces (exerted by membrane-attached minus-end-directed motor proteins). It is certainly feasible to include both effects in a future version of these models. The second one, and closely related to the first, is the neglect of MT buckling. The simplest way to partially include this effect was pioneered in Ref. [5] and consists of fixing the force exerted by the MTs to be equal to the (length-dependent) buckling force. The latter assumption, however, presupposes that the dimensions of the cell are comparable to the buckling length given the known magnitude of the polymerization forces, and therefore less robust to scaling of the size of the cell. This effect could be partially remedied by using our force production model, or a variant such as the one proposed in Ref. [25], and cap the force to the buckling force if this reached before the switch to the shrinking state. However, as MTs do not physically buckle in any of these variants, we believe the results might be quantitatively different, but not qualitatively. In all cases one would observe more or less uniform sliding towards the longitudinal axis of the cell. Including true physical buckling, in which the postbuckling orientation with respect to the cell boundary also becomes salient, is much more challenging, and would require significantly more complex calculations. Finally, the choice for a two-dimensional geometry. While we have argued that for symmetry reasons this is reasonable approximation, it should be both feasible and useful to extend our calculations to more general 3D cell shapes. The analytical theory in model M0, which only requires the orientation-dependent distance from the MTOC to the cell boundary as input, is readily generalized, especially in the axially symmetric case. The same holds for the simulations, albeit more care has to be taken to avoid orientational artifacts due to nonisotropic sampling of orientations and the homogeneity and isotropicity of the surface mesh that keeps track of the bound MTs and the diffusing PFs.

Returning to the biological significance of our results, we note that while there is a surprising variety of ordered MT structures in animal cells (for a recent review see [28]) and many of the cell types involved are distinctly nonspherical in shape, the dominant explanatory principles employed in discussing the origin of these structures are the spatial location of the nucleation sites (e.g., centrosomal or noncentrosomal and localized to specific cell faces), selective modulation of microtubule dynamics, the mechanical action of motor proteins (see, e.g., [29] for the case of neurons), and polarization mechanisms such as the one introduced in our model MP. Strikingly, the effect of the cell geometry in shaping these distributions in the first place appears to be disregarded. The proposed mechanisms are generically good at explaining the *maintenance* of a specific structure once it has been established, but often beg the question of its *creation*. We hope that our work provides a starting point for a reappraisal of the role of geometrical confinement and how this interacts with other mechanisms in shaping MT organization. A case in point is our result that in the absence of other factors the dominant form of induced polarization is predicted to select the shortest axis available in the cell, in contrast to the predominantly longitudinal organization found in elongated cells. Here we show that polymerization-driven sliding is an effective reorienting mechanisms that exploits the anisotropic nature of the confining cell geometry. Finally, our results show that mechanisms involving feedback loops based on PFs that are transported by MTs to the cell boundary, predominantly create a uniaxial polar structure, in spite of strong geometrical cues towards a biaxial organization. It is therefore an interesting question from a fundamental point of view whether it is possible to create a polarization mechanism, likely involving at least two polarity factors, that supports biaxial polarization even in the absence of the sliding mechanism. The latter could

contribute to our understanding of the longitudinal biaxial MT organization found, e.g., in fission yeast.

ACKNOWLEDGMENTS

We thank Alex Cumberworth (AMOLF) for his critical reading of the manuscript. This work is part of the research programme of the Netherlands Organisation for Scientific Research (NWO) and was performed at the research institute AMOLF.

APPENDIX A: DERIVATION STATE-STEADY EQUATIONS MODEL M0

In order to derive the steady-state equations for the MT length distributions for model M0, we start from the time-dependent equations. For the active and bound MTs these read

$$\partial_t m_+(l,\varphi,t) = -v_+\partial_l m_+(l,\varphi,t) + r_- m_-(l,\varphi,t) - r_+ m_+(l,\varphi,t), \tag{A1}$$

$$\partial_t m_-(l,\varphi,t) = v_-\partial_l m_-(l,\varphi,t) - r_- m_-(l,\varphi,t) + r_+ m_+(l,\varphi,t), \tag{A2}$$

$$\partial_t m_\mathrm{b}(\varphi,t) = -r_\mathrm{u} m_\mathrm{b}(\varphi,t) + v_+ m_+(l_\mathrm{b}(\varphi),\varphi,t). \tag{A3}$$

The equations for the dormant ones now depend on the chosen nucleation scenario. For the homogeneous scenario there is a density $m_0(\varphi,t)$ of dormant MTs per angle, while in the random scenario there is just a single pool of dormant MTs $M_0(t)$. We thus have

$$\partial_t m_0(\varphi,t) = -r_\mathrm{n} m_0(\varphi,t) + v_- m_-(l=0,\varphi,t), \tag{A4a}$$

$$d_t M_0(t) = -r_\mathrm{n} M_0(t) + v_- \int_0^{2\pi} d\varphi\, m_-(l=0,\varphi,t), \tag{A4b}$$

where throughout the a-sublabeled equations will refer to the homogeneous case, and the b-sublabeled ones to the random case. These equations need to be supplemented with boundary conditions. At the cell boundary these are

$$r_\mathrm{u} m_\mathrm{b}(\varphi,t) = v_- m_-(l_\mathrm{b}(\varphi),\varphi,t), \tag{A5}$$

while at $l=0$ they again depend on the nucleation scenario

$$v_+ m_+(l=0,\varphi,t) = r_\mathrm{n} m_0(\varphi,t), \tag{A6a}$$

$$v_+ m_+(l=0,\varphi,t) = \frac{1}{2\pi} r_\mathrm{n} M_0(t). \tag{A6b}$$

We now introduce a number of integrated quantities. First, the total number of growing, shrinking, and *active* MTs in a given direction in the interior,

$$m_+(\varphi,t) = \int_0^{l_\mathrm{b}(\varphi)} dl\, m_+(l,\varphi,t), \tag{A7}$$

$$m_-(\varphi,t) = \int_0^{l_\mathrm{b}(\varphi)} dl\, m_-(l,\varphi,t), \tag{A8}$$

$$m_\mathrm{a}(\varphi,t) = m_+(\varphi,t) + m_-(\varphi,t), \tag{A9}$$

and next the total number of active and bound MTs in the system

$$M_\mathrm{a}(t) = \int_0^{2\pi} d\varphi\, m_\mathrm{a}(\varphi,t), \tag{A10}$$

$$M_\mathrm{b}(t) = \int_0^{2\pi} d\varphi\, m_\mathrm{b}(\varphi,t). \tag{A11}$$

Adding Eqs. (A1) and (A2) and integrating over the relevant lengths yields

$$\partial_t m_\mathrm{a}(\varphi,t) = [v_- m_-(l_\mathrm{b}(\varphi),\varphi,t) - v_+ m_+(l_\mathrm{b}(\varphi),\varphi,t)] - [v_- m_-(l=0,\varphi,t) - v_+ m_+(l=0,\varphi,t)]. \tag{A12}$$

Adding this identity to Eq. (A3) and taking into account Eq. (12) then gives

$$\partial_t m_\mathrm{a}(\varphi,t) + \partial_t m_\mathrm{b}(\varphi,t) = v_+ m_+(l=0,\varphi,t) - v_- m_-(l=0,\varphi,t). \tag{A13}$$

For the homogeneous nucleation scenario, this can immediately be combined with Eq. to yield

$$\partial_t m_0(\varphi,t) + \partial_t m_\mathrm{a}(\varphi,t) + \partial_t m_\mathrm{b}(\varphi,t) = 0, \tag{A14}$$

while for the random scenario, we first need to integrate Eq. (A13) over all angles, and then combine with Eqs. and to get

$$\frac{d}{dt}[M_0(t) + M_\mathrm{a}(t) + M_\mathrm{b}(t)] = 0, \tag{A15}$$

which given our definitions lead to the conservation equations

$$m = m_0(\varphi,t) + m_\mathrm{a}(\varphi,t) + m_\mathrm{b}(\varphi,t), \tag{A16a}$$

$$M = M_0(t) + M_\mathrm{a}(t) + M_\mathrm{b}(t). \tag{A16b}$$

The steady-state equations used in the main text now follow by assuming all unknowns are independent on time.

APPENDIX B: VALIDATION OF THE MT LENGTH DISTRIBUTION AS MEASURED IN THE SIMULATIONS

We compare the MT length distribution as measured in the simulations to the analytical predictions following from Eqs. (30) for both nucleation scenarios in model M0. Figure 12 shows the high level of agreement achieved. Error bars in these simulations are smaller than the plotting symbols. That the order parameter values are then also accurately reproduced is shown in the right panel of Fig. 3.

APPENDIX C: CENTERING FORCE IN MODEL MS

To check whether it is reasonable to assume that the central position of the MTOC is stable in model MS (and by extension in model MSP) where forces are exerted by the MTs, we performed simulations in which the MTOC was displaced along the long axis and measured the resultant average force on the MTOC. As the results shown in Fig. 13 show, we find that in all cases there is a robust restoring force that increases with increasing distance from the center.

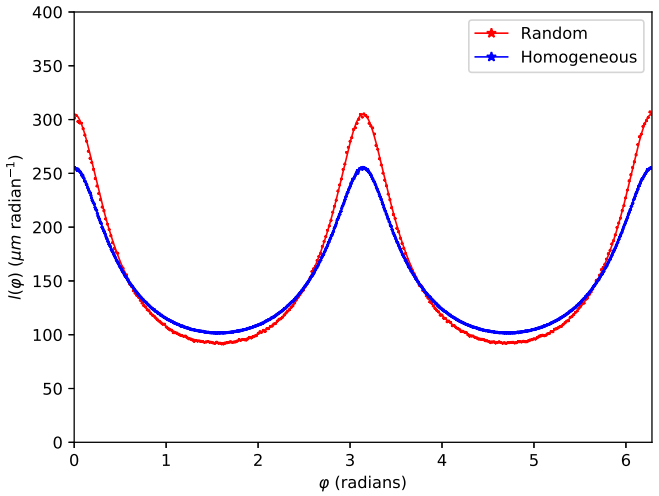

FIG. 12. Model M0: Length distribution $l(\varphi)$. Solid lines: theoretical prediction, symbols: simulations, for the random nucleation scenario (red symbols) and the the homogeneous scenario (blue symbols). Parameters: long semiaxis $b = 4\,\mu\text{m}$, $r_\text{u} = 0.01\,\text{s}^{-1}$, average taken over 20×10^6 time steps.

APPENDIX D: PF DENSITY-DEPENDENT CATASTROPHE RATE IN MODEL MSP

We implement the influence of the PFs on the force-dependent catastrophe mechanism of model MS through the unloaded catastrophe rate r_+ by making it dependent on the PF density through imposing the constraint Eq. (42). To that end we use the previously determined for the compression modulus $k = 0.3\,\text{pN}\mu\text{m}^{-1}$ and unloaded growth speed $v_+ = 0.018\,\mu\text{ms}^{-1}$, and take the unloaded catastrophe rate $r_+(c_\text{b} = 0) = 0.0078\,\text{s}^{-1}$, which matches the value of $r_\text{u} = 0.01\,\text{s}^{-1}$, i.e., $\langle\tau_\text{c}\rangle(c_\text{b} = 0) = 100\,\text{s}$, used in model MP. Using these values, we then solve Eq. (42) for a range of c_b values. We show the results after translating the density to a number of PFs per length bin on the surface in the simulation for the case $c_* = 60$ in Fig. 14.

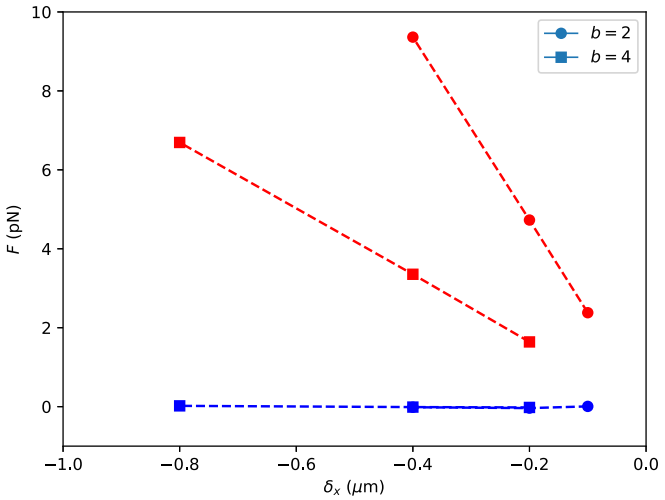

FIG. 13. Longitudinal (red) and transverse (blue) components of the average force on the MTOC, when displaced to the left of the origin along the x axis, by an amount δ_x in two geometries, showing that there is a net restoring force to the geometrical center.

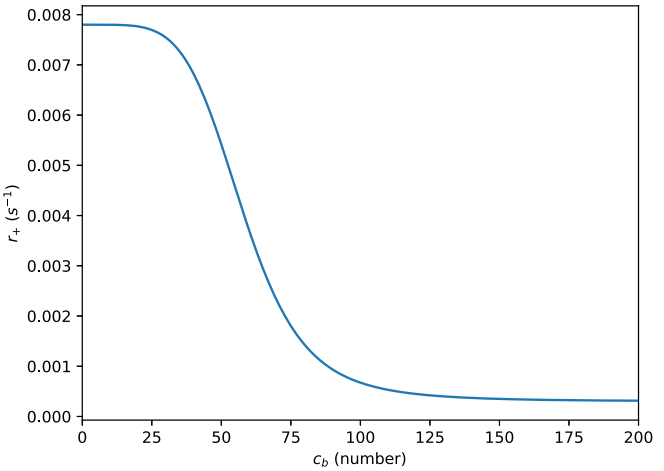

FIG. 14. Force-free catastrophe rate r_+ (in s^{-1}) as a function of the number of polarity factors c_b per simulation bin at the cell boundary.

APPENDIX E: TOY MODEL OF THE POLARIZATION MECHANISM

1. Assumptions

We develop a simple and analytically tractable toy model to aid the analysis of the results of the two models that involve the polarization mechanism, Model MP (Sec. III C) and Model MSP (Sec. III D). The first simplifying assumption is to focus exclusively on the competition between the shorter transverse axis, with length scale a and the longer longitudinal axis with length scale $b > a$. Instead of considering isotropically nucleated MTs, we therefore consider a discrete direction model where MTs are nucleated only in the directions $\varphi = 0$ and $\varphi = \pi$, corresponding to the longitudinal direction, and $\varphi = \pi/2$ and $\varphi = 3\pi/2$, corresponding to the transverse direction. The second assumption is that if the diffusion length of the PFs in the membrane, which is given by $\lambda = \sqrt{D/k_u}$ is small compared to a quarter of the circumference of the cell, we can neglect the diffusional cross-talk between PFs delivered at different sites because the membrane is closed. MTs in each of the discrete direction thus deliver their PFs to their own unbounded membrane, from which they can subsequently unbind to return to the cell interior. In case the sliding mechanism is also present, we assume that all MTs rapidly slide to the poles, so that effectively we only need to consider MTs nucleated in the two longitudinal directions. Finally, instead of fixing the total number of MTs, we specify only their rate of nucleation, which we take to be isotropic, i.e., corresponding to the homogeneous nucleation scenario. Although not essential, this latter assumption greatly simplifies the analysis. This toy model is illustrated in Fig. 15.

2. General formulation

In general our toy model can have N different discrete directions labeled by an index $i = 0, 1, \ldots, N-1$,

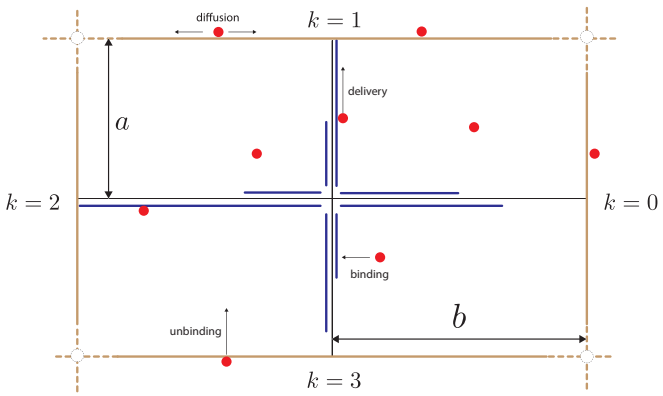

FIG. 15. Schematic of the toy model for the polarization mechanism. Microtubules (blue lines) are nucleated in four directions ($k = 0, 1, 2, 3$) towards the edges of a square. Polarity factors (red circles) bind to the microtubules and are delivered by them to the four boundaries, where they diffuse until they unbind back to the interior.

corresponding to the spatial directions $\varphi = \frac{2\pi}{n} i$. The distance from the central MTOC to the boundary in the different directions is given by d_i. Assuming we are in steady state, the relevant variables are the MT length densities $m_i^{\pm}(l)$, the number of membrane-bound MTs M_i^{b} and the local PFdensities $c_i^{\mathrm{b}}(s_i)$, where s_i is a signed distance coordinate in the membrane connected to the direction i. The unbinding rate of MTs is given by Eq. (40) evaluated in $c_i^{\mathrm{b}}(s_i = 0)$. The nucleation rate of new MTs is given by r_{n} *per direction*. Denoting the value of the MT unbinding rate by $r_{u,i}$, which we note is a quantity that needs to be self-consistently determined, the solutions of the steady-state MT densities is simply given by (cf. Appendix A and Sec. III A)

$$m_i^{+}(l) = \frac{r_{\mathrm{n}}}{v_+} e^{-l/\bar{l}}, \tag{E1}$$

$$m_i^{-}(l) = \frac{r_{\mathrm{n}}}{v_-} e^{-l/\bar{l}}, \tag{E2}$$

$$M_i^{\mathrm{b}} = \frac{v_+}{r_{u,i}} m_i^{+}(d_i) = \frac{r_{\mathrm{n}}}{r_{u,i}} e^{-d_i/\bar{l}} \equiv \frac{r_{\mathrm{n}}}{r_{u,i}} F_i. \tag{E3}$$

A key quantity in our model is the total length of MTs in the direction i

$$L_i = \int_0^{d_i} dl\, l[m_i^{+}(l) + m_i^{-}(l)] + d_i M_i^{\mathrm{b}}, \tag{E4}$$

$$= r_{\mathrm{n}} \bar{l}[\bar{l}(1 - F_i) - d_i F_i] + d_i M_i^{\mathrm{b}}, \tag{E5}$$

and its total $L = \sum_i L_i$.

Turning to the PF dynamics, we first define the total number of bound PFs per direction

$$C_i^{\mathrm{b}} = \int_{-\infty}^{\infty} ds_i\, c_i^{\mathrm{b}}(s_i), \tag{E6}$$

and the total number of bound PFs $C^{\mathrm{b}} = \sum_i C_i^{\mathrm{b}}$. The density per unit length of MT-bound PFs in the cell the follows from Eq. (39)

$$c^{\mathrm{m}} = \frac{1}{L + L_{\frac{1}{2}}} (C - C^{\mathrm{b}}). \tag{E7}$$

The net flux of PFs reaching the membrane in the direction i is thus

$$K_i^{\mathrm{b}} = v_{\mathrm{m}} c^{\mathrm{m}} M_i^{\mathrm{b}}. \tag{E8}$$

In steady state, the PF density in this membrane satisfies

$$D \frac{d^2}{ds^2} c_i^{\mathrm{b}}(s) - k_{\mathrm{u}} c_i^{\mathrm{b}}(s) + K_i^{\mathrm{b}} \delta(s) = 0, \tag{E9}$$

with solution

$$c_i^{\mathrm{b}}(s) = \frac{1}{2} \frac{K_i^{\mathrm{b}}}{\ell k_{\mathrm{u}}} e^{-|s|/\ell}, \tag{E10}$$

where the free diffusion length is given by $\ell = \sqrt{D/k_{\mathrm{u}}}$. The total number of PFs in this membrane is then simply $C_i^{\mathrm{b}} = K_i^{\mathrm{b}}/k_{\mathrm{u}}$ and $c_i^{\mathrm{b}}(0) = \frac{1}{2} C_i^{\mathrm{b}}/\ell$.

We now nondimensionalize by choosing r_{n}^{-1} as unit of time and $\bar{l}$ as unit of length, introducing $\Lambda = L/\bar{l}$, $\delta_i = d_i/\bar{l}$, $\bar{\tau} = \bar{t} r_{\mathrm{n}}$. We also introduce C_*, the cross-over number of PFs through $c_* = \frac{1}{2} C_*/\ell$, and use this as a unit of measurement for PFs, introducing $\Gamma_i = C_i^{\mathrm{b}}/C_* = c_i^{\mathrm{b}}(0)/c_*$. This allows us to write

$$\frac{K_i^{\mathrm{b}}}{k_{\mathrm{u}} C_*} = \omega \frac{1}{\Lambda(\{\Gamma_j\}) + \Lambda_*} \left(\Gamma - \sum \Gamma_j \right) M_i^{\mathrm{b}}(\Gamma_i) = \Gamma_i, \tag{E11}$$

where $\omega = v_{\mathrm{m}}/(k_{\mathrm{u}} \bar{l})$. We note that

$$\Lambda_j(\Gamma_j) = \bar{\tau}[(1 - F_i) - \delta_i F_i] + \delta_i M_i^{\mathrm{b}}(\Gamma_j), \tag{E12}$$

so that

$$\Lambda(\{\Gamma_j\}) = \bar{\tau} \left(\sum_i (1 - F_i) - \delta_i F_i \right) + \sum_i \delta_i M_i^{\mathrm{b}}(\Gamma_i). \tag{E13}$$

Introducing $\Lambda_0 = \bar{\tau}[\sum_i (1 - F_i) - \delta_i F_i] + \Lambda_*$ we can rewrite (E11) as

$$\omega \frac{M_i^{\mathrm{b}}(\Gamma_i)}{\Lambda_0 + \sum_j \delta_j M_j^{\mathrm{b}}(\Gamma_j)} = \frac{\Gamma_i}{\Gamma - \sum \Gamma_j}. \tag{E14}$$

Multiplying by δ_i and summing allows us to solve for

$$\sum_j \delta_j M_j^{\mathrm{b}}(\Gamma_j) = \frac{\Lambda_0 \sum_j \delta_j \Gamma_j}{\omega \Gamma - \sum_j (\omega + \delta_j) \Gamma_j}. \tag{E15}$$

This in turn allows us to solve for

$$M_i^{\mathrm{b}}(\Gamma_i) = \Lambda_0 \frac{\Gamma_i}{\omega \Gamma - \sum_j (\omega + \delta_j) \Gamma_j}. \tag{E16}$$

Next, in Eq. (40) we introduce $\rho = r_{\mathrm{u}}(0)/r_{\mathrm{u}}(\infty) > 1$ and write

$$r_{\mathrm{u}}\left[c_i^{\mathrm{b}}(0)\right] = r_{\mathrm{u}}(\infty) \frac{\rho + \Gamma_i^p}{1 + \Gamma_i^p} \equiv r_{\mathrm{u}}(\infty) R(\Gamma_i). \tag{E17}$$

This allows us to compactly formulate the remaining boundary conditions (E3)

$$\frac{r_{\mathrm{n}}}{r_{\mathrm{u}}(\infty)} F_i = R(\Gamma_i) M_i^{\mathrm{b}}(\Gamma_i). \tag{E18}$$

Using this to eliminate $M_i^{\mathrm{b}}(\Gamma_i)$ from (E16), then yields our final equations

$$U_i = \frac{R(\Gamma_i)\Gamma_i}{\omega \Gamma - \sum_j (\omega + \delta_j) \Gamma_j}, \tag{E19}$$

where the constants on the left-hand side are given by

$$U_i = \frac{r_n}{\Lambda_0 r_u(\infty)} F_i > 0. \tag{E20}$$

For the further analysis it is useful to define the denominator of (E19) as a separate function $W(\{\Gamma_j\}) = \omega\Gamma - \sum_j (\omega + \delta_j)\Gamma_j$ and note that is satisfies the bounds $0 < W(\{\Gamma_j\}) \leqslant \omega\Gamma$ and is monotonically decreasing in each of its variables in the physical domain $\Gamma_j \geqslant 0$. The function in the numerator $R(\Gamma)\Gamma \geqslant 0$ has an inflexion point and two local extrema whenever $\rho > [(p+1)/(p-1)]^2$ and diverges as $\Gamma \to \infty$, so its inverse can be multivalued over a finite range.

3. Models TOY-MP and TOY-MSP

In the case intended to mimic Model MP, we have four discrete directions, corresponding to the two longitudinal orientations $\varphi = 0$ and $\varphi = \pi$ and the two transverse directions $\varphi = \pi/2$ and $\varphi = 3\pi/2$. We define $\beta = \delta_0 = \delta_2 = b/\bar{l}$ and $\alpha = \delta_1 = \delta_3 = a/\bar{l}$, $U_\beta = U_0 = U_2$ and $U_\alpha = U_1 = U_3$, noting that $U_\beta < U_\alpha$ as $b > a$, and $W(\Gamma_0 + \Gamma_2, \Gamma_1 + \Gamma_3) = \omega\Gamma - (\omega + \beta)(\Gamma_0 + \Gamma_2) - (\omega + \alpha)(\Gamma_1 + \Gamma 3)$. We can then write the self-consistency equations (E19) in this case as

$$W(\Gamma_0 + \Gamma_2, \Gamma_1 + \Gamma_3)U_\beta = R(\Gamma_0)\Gamma_0 = R(\Gamma_2)\Gamma_2, \tag{E21}$$

$$W(\Gamma_0 + \Gamma_2, \Gamma_1 + \Gamma_3)U_\alpha = R(\Gamma_1)\Gamma_1 = R(\Gamma_3)\Gamma_3. \tag{E22}$$

WLOG, we can also require $\Gamma_0 \geqslant \Gamma_2$ and $\Gamma_1 \geqslant \Gamma_3$ as this simply divides out the multiplicity due to the trivial interchange symmetries $\Gamma_0 \leftrightarrow \Gamma_2$ and $\Gamma_1 \leftrightarrow \Gamma_3$.

This allows the following systematic algorithm to find all possible solutions:

Step 1: Choose a $w \in [0, \omega\Gamma]$. Solve

$$R(\Gamma_0)\Gamma_0 = R(\Gamma_2)\Gamma_2 = wU_\beta, \tag{E23}$$

$$R(\Gamma_1)\Gamma_1 = R(\Gamma_3)\Gamma_3 = wU_\alpha. \tag{E24}$$

As $R(\Gamma)\Gamma$ is a universal function, which is either monotonic, or has two local extrema, and values on $[0, \infty)$ these two equations always have solutions, which can in principle be of the types (i) $\Gamma_0 = \Gamma_2$ and $\Gamma_1 = \Gamma_3$, the default biaxial reference solution, (ii) $\Gamma_0 = \Gamma_2$ and $\Gamma_1 > \Gamma_3$, which we call transversely polarized, (iii) $\Gamma_0 > \Gamma_2$ and $\Gamma_1 = \Gamma_3$, which we call longitudinally polarized, and finally (iv) $\Gamma_0 > \Gamma_2$ and $\Gamma_1 > \Gamma_3$, which we would call doubly polarized. Note that in case of multiple solutions of $R(\Gamma)\Gamma =$ constant, we discard the unstable middle solution for which $R'(\Gamma)\Gamma + R(\Gamma) < 0$.

Step 2: Next we check if $W(\Gamma_1 + \Gamma_3, \Gamma_2 + \Gamma_3) = w$. If yes, a self-consistent solution is found, if not, choose another w. Since the solutions $[\Gamma_1(w), \Gamma_3(w), \Gamma_2(w), \Gamma_4(w)]$ are readily determined, this procedure boils down to the one-dimensional self-consistency problem

$$w = W[\Gamma_1(w) + \Gamma_3(w), \Gamma_2(w) + \Gamma_3(w)] \tag{E25}$$

on $w \in [0, \omega\Gamma]$, which is guaranteed to have one solution (the default solution (i) above), but may have more.

As order parameters we take the discrete analogs of the order parameters defined in Sec. II A:

$$\mathbf{S}_{1,x} = \frac{\sum_{i=0}^3 L_i \cos\frac{\pi}{2} i}{\sum_{i=0}^3 L_i} = \frac{L_0 - L_2}{L_0 + L_1 + L_2 + L_3}, \tag{E26}$$

$$\mathbf{S}_{1,y} = \frac{\sum_{i=0}^3 L_i \sin\frac{\pi}{2} i}{\sum_{i=0}^3 L_i} = \frac{L_1 - L_3}{L_0 + L_1 + L_2 + L_3}, \tag{E27}$$

$$S_2 = \frac{\sum_{i=0}^3 L_i \cos\pi i}{\sum_{i=0}^3 L_i} = \frac{(L_0 + L_2) - (L_1 + L_3)}{L_0 + L_1 + L_2 + L_3}. \tag{E28}$$

In the case intended to mimic Model MSP we have only two directions, corresponding to the two longitudinal orientations $\varphi = 0$ and $\varphi = \pi$. In this case we have $W(\Gamma_0 + \Gamma_2) = \omega\Gamma - (\omega + \beta)(\Gamma_0 + \Gamma_2)$, with $\Omega = \omega\Gamma/(\omega + \beta)$ and $V = (\omega + \beta)U_\beta$, and the self-consistency equations become

$$W(\Gamma_0 + \Gamma_2)U_\beta = R(\Gamma_0)\Gamma_0 = R(\Gamma_2)\Gamma_2. \tag{E29}$$

The only order parameter relevant to this case is $\mathbf{S}_{1,x}$, as $\mathbf{S}_{1,y} = 0$ and $S_2 = 1$ by construction.

From symmetry it is clear that (E29) admits a biaxial "reference" solution of the form $\Gamma^{(0)} = \Gamma_0 = \Gamma_2$ satisfying

$$W(2\Gamma^{(0)})V = R(\Gamma^{(0)})\Gamma^{(0)}. \tag{E30}$$

Although we would like to study the solutions of this equation as a function of Ω, which through its linear dependence on Γ is a proxy for the total amount of PFs in the system, it is actually simpler to study the inverse problem, and consider

$$\Omega(\Gamma^{(0)}) = \frac{1}{V}[2V\Gamma^{(0)} + R(\Gamma^{(0)})\Gamma^{(0)}]. \tag{E31}$$

Taking the derivative with respect to $\Gamma^{(0)}$, here denoted by a prime, we find

$$\Omega'(\Gamma^{(0)}) = \frac{1}{V}\{2V + [R(\Gamma^{(0)})\Gamma^{(0)}]'\}. \tag{E32}$$

As $V > 0$ this shows that $\Gamma^{(0)}(\Omega)$ can be multivalued only if $R(\Gamma^{(0)})\Gamma^{(0)}$ is nonmonotonic.

[1] K. Barlan and V. I. Gelfand, Cold Spring Harbor Persp. Biol. **9**, a025817 (2017).

[2] J. Wu and A. Akhmanova, Annu. Rev. Cell Dev. Biol. **33**, 51 (2017).

[3] D. Oriola, D. J. Needleman, and J. Brugués, Annu. Rev. Biophys. **47**, 655 (2018).

[4] P. T. Tran, L. Marsh, V. Doye, S. Inoué, and F. Chang, J. Cell Biol. **153**, 397 (2001).

[5] L. Laan, N. Pavin, J. Husson, G. Romet-Lemonne, M. van Duijn, M. P. López, R. D. Vale, F. Jülicher, S. L. Reck-Peterson, and M. Dogterom, Cell **148**, 502 (2012).

[6] L. Laan, S. Roth, and M. Dogterom, Cell Cycle **11**, 3750 (2012).

[7] J. L. Meaders, S. N. de Matos, and D. R. Burgess, Cell Rep. **33**, 108213 (2020).

[8] A. J. Jimenez, A. Schaeffer, C. De Pascalis, G. Letort, B. Vianay, M. Bornens, M. Piel, L. Blanchoin, and M. Théry, Curr. Biol. **31**, 1206 (2021).
[9] N. Pavin, L. Laan, R. Ma, M. Dogterom, and F. Jülicher, New J. Phys. **14**, 105025 (2012).
[10] R. Ma, L. Laan, M. Dogterom, N. Pavin, and F. Jülicher, New J. Phys. **16**, 013018 (2014).
[11] T. Lechler and M. Mapelli, Nat. Rev. Mol. Cell Biol. **22**, 691 (2021).
[12] B. J. Thompson, Development **140**, 13 (2013).
[13] J. Mata and P. Nurse, Cell **89**, 939 (1997).
[14] D. Brunner and P. Nurse, Cell **102**, 695 (2000).
[15] P. Recouvreux, T. R. Sokolowski, A. Grammoustianou, P. R. ten Wolde, and M. Dogterom, Proc. Natl. Acad. Sci. USA **113**, 1811 (2016).
[16] P. Foteinopoulos and B. M. Mulder, PLoS ONE **12**, e0184706 (2017).
[17] J. Teapal, L. J. Schuitman, B. M. Mulder, and M. E. Janson, Eur. Phys. J. Plus **136**, 858 (2021).
[18] M. Dogterom and S. Leibler, Phys. Rev. Lett. **70**, 1347 (1993).
[19] X. Su, H. Arellano-Santoyo, D. Portran, J. Gaillard, M. Vantard, M. Thery, and D. Pellman, Nat. Cell. Biol. **15**, 948 (2013).
[20] J. Vogel, B. Drapkin, J. Oomen, D. Beach, K. Bloom, and M. Snyder, Dev. Cell **1**, 621 (2001).
[21] M. Dogterom, J. W. J. Kerssemakers, G. Romet-Lemonne, and M. E. Janson, Curr. Opin. Cell Biol. **17**, 67 (2005).
[22] M. E. Janson, M. E. de Dood, and M. Dogterom, J. Cell Biol. **161**, 1029 (2003).
[23] C. S. Peskin, G. M. Odell, and G. F. Oster, Biophys. J. **65**, 316 (1993).
[24] M. Dogterom and B. Yurke, Science **278**, 856 (1997).
[25] D. Foethke, T. Makushok, D. Brunner, and F. J. Nédélec, Mol. Syst. Biol. **5**, 241 (2009).
[26] I. S. Gradshteyn and I. M. Ryzhik, *Table of Integrals, Series, and Products*, 7th ed., edited by A. Jeffrey and D. Zwillinger (Academic Press, San Diego, 2007).
[27] A. Jilkine and L. Edelstein-Keshet, PLoS Comput. Biol. **7**, e1001121 (2011).
[28] A. Akhmanova and L. C. Kapitein, Nat. Rev. Mol. Cell Biol. **23**, 541 (2022).
[29] L. C. Kapitein and C. C. Hoogenraad, Neuron **87**, 492 (2015).